

PAPER • OPEN ACCESS

HIFU-induced changes in optical scattering and absorption of tissue over nine orders of thermal dose

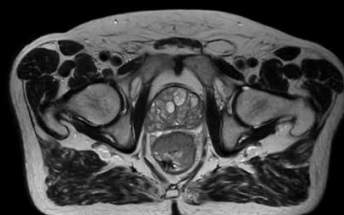
To cite this article: Jason L Raymond *et al* 2018 *Phys. Med. Biol.* **63** 245001

View the [article online](#) for updates and enhancements.

Uncompromised.

See clearly during treatment to attack the tumor and protect the patient.

Two worlds, one future.



Captured on Elekta high-field MR-linac during 2018 imaging studies.

 **Elekta**

Elekta MR-linac is pending FDA premarket clearance and not available for commercial distribution or sale in the U.S.

OPEN ACCESS



CrossMark

RECEIVED
16 July 2018REVISED
29 October 2018ACCEPTED FOR PUBLICATION
1 November 2018PUBLISHED
7 December 2018

Original content from
this work may be used
under the terms of the
[Creative Commons
Attribution 3.0 licence](#).

Any further distribution
of this work must
maintain attribution
to the author(s) and the
title of the work, journal
citation and DOI.



PAPER

HIFU-induced changes in optical scattering and absorption
of tissue over nine orders of thermal doseJason L Raymond^{1,3} , Robin O Cleveland^{1,2} and Ronald A Roy¹¹ Department of Engineering Science, University of Oxford, Parks Road, Oxford OX1 3PJ, United Kingdom² Institute of Biomedical Engineering, University of Oxford, Old Road Campus Research Building, Oxford OX3 7DQ, United Kingdom³ Author to whom any correspondence should be addressed.E-mail: jason.raymond@eng.ox.ac.uk**Keywords:** high-intensity focused ultrasound, thermal dose, optical properties, thermal damage, lesion

Abstract

The optical properties of tissue change during thermal ablation. Multi-modal methods such as acousto-optic (AO) and photo-acoustic (PA) imaging may provide a real-time, direct measure of lesion formation. Baseline changes in optical properties have been previously measured over limited ranges of thermal dose for tissues exposed to a temperature-controlled water bath, however, there is scant data for optical properties of lesions created by HIFU. In this work, the optical scattering and absorption coefficients from 400–1300 nm of excised chicken breast exposed to HIFU were measured using an integrating sphere spectrophotometric technique. HIFU-induced spatiotemporal temperature elevations were measured using an infrared camera and used to calculate the thermal dose delivered to a localized region of tissue. Results obtained over a range of thermal dose spanning 9 orders of magnitude show that the reduced scattering coefficient increases for HIFU exposures exceeding a threshold thermal dose of $\text{CEM}_{43} = 600 \pm 81$ cumulative equivalent minutes. HIFU-induced thermal damage results in changes in scattering over all optical wavelengths, with a 2.5-fold increase for thermal lesions exceeding 70 °C. The tissue absorption coefficient was also found to increase for thermally lesioned tissue, however, the magnitude was strongly dependent on the optical wavelength and there was substantial sample-to-sample variability, such that the existence of a threshold thermal dose could not be determined. Therapeutic windows, where the optical penetration depth is expected to be greatest, were identified in the near infrared regime centered near 900 nm and 1100 nm. These data motivate further research to improve the real-time AO and PA sensing of lesion formation during HIFU therapy as an alternative to thermometry.

1. Introduction

Tissue heating and thermal ablation using high intensity focused ultrasound (HIFU) is being adopted in the clinic as a non-invasive surgical technique for treatment of solid tumors in cancer (Hsiao *et al* 2016) and non-malignant ablative therapies (Chen *et al* 2017, Lang *et al* 2017). In HIFU, high amplitude ultrasound waves are focused to a target location and the absorption of acoustic energy elevates the tissue temperature, resulting in thermal ablation of a cigar-shape region of tissue typically 1–3 mm in diameter and 1–2 cm in length. One of the barriers to wider deployment of HIFU is that it is difficult to ensure adequate energy has been delivered to tissue for treatment guidance and verification.

Magnetic resonance (MR) imaging is considered the ‘gold standard’ for guiding and monitoring HIFU by thermometry (Kim 2015, Zhu *et al* 2017) and is able to accurately estimate the temperature changes in tissue, however, it does not directly measure absolute temperature or lesion formation and a thermal dose model is needed to infer tissue ablation based on spatial maps of relative temperature increase due to HIFU (McDannold 2005, Rivens *et al* 2007). MR-based elastography methods such as acoustic radiation force imaging (MR-ARFI) may be useful for monitoring irreversible changes in tissue elasticity due to HIFU treatment but have so far only

been implemented off-line (Vappou *et al* 2018). Drawbacks of MRI techniques include the limited temporal and spatial resolution, the requirement that the ultrasound equipment be MR-compatible, and the high cost of MRI systems.

Ultrasound has long been used for guiding HIFU therapy due to the low-cost and relative simplicity of coupling an ultrasonic imaging transducer with HIFU (Frenkel 2010). Methods which generate differential maps of the changes in tissue attenuation (Ribault *et al* 1998), or backscatter energy (Ribault *et al* 1998, Seip *et al* 2002, Zhong *et al* 2007) have been utilized with some success and such tissue-change monitoring techniques have been verified recently in clinical studies of HIFU prostate ablation (Sanghvi *et al* 2017). Along the same lines, echo decorrelation imaging has been validated for prediction of thermal lesioning *in vivo* (Fosnight *et al* 2017, Abbass *et al* 2018). Ultrasound elastographic techniques (Righetti *et al* 1999, Shi *et al* 1999, Souchon *et al* 2003) including acoustic radiation-force imaging (Bing *et al* 2011) and harmonic motion imaging (Han *et al* 2017) have been investigated. Overall, the lack of both sufficient contrast between healthy and lesioned tissue and robust processing techniques means that despite some progress being made, ultrasound monitoring has yet to supplant MR guidance in clinical applications.

The work reported here is motivated by the possibility of exploiting the change in optical properties that occur with heating and lesion formation (Jacques and Gaeni 1989) in order to sense tissue changes through the interaction of light and sound. For example, an increase in the optical absorption after lesion formation should result in an increase in photoacoustic (PA) signal generation (Cui and Yang 2011, Gray *et al* 2016). Similarly, acousto-optic (AO) sensing, which is sensitive to both optical absorption and scattering, has been shown to non-invasively detect changes in *ex vivo* tissue optical properties during HIFU exposures in real-time (Lai *et al* 2011, Murray *et al* 2012).

Although there are measurements of the changes in tissue optical properties induced by heating in water baths (Agah *et al* 1996, Adams *et al* 2014, Zhao *et al* 2018) and by the absorption of laser light (Ritz *et al* 2001), there is limited data quantifying optical property changes in response to HIFU-induced thermal lesion formation. Changes in optical properties have been measured for HIFU-treated chicken breast (Alhamami *et al* 2014), although only for complete coagulation and not as a function of energy or thermal dose delivered to the tissue.

The aim of this study was to determine the optical absorption and reduced scattering coefficients of a model tissue between 400 and 1300 nm and the changes in these properties caused by HIFU-induced heating and lesion formation. A sector-vortex lens was fitted to the HIFU source in order to produce a region of relatively uniform exposure sufficient to enable the accurate measurement of optical properties. A thermal camera was employed to visualize the temperature field and calculate the time-dependent and spatially-averaged thermal dose. The wavelength-dependent total transmittance and reflectance of the tissue samples were measured using a dual-beam spectrometer equipped with an integrating sphere. This data, when combined with the known tissue sample thickness, yielded the wavelength-dependent optical scattering and absorption coefficients of the tissue samples.

2. Materials and methods

2.1. Sample preparation

Tissue samples were prepared following the methods of Çilesiz and Welch (1993) and Adams *et al.* (2014). Fresh chicken breast acquired from a local supermarket was refrigerated and used before the expiration date on the package. A commercial meat slicer (GH489; Caterlite, Bristol, UK) was used to section the tissue into samples of approximately 2 mm thickness, which were trimmed to approximately 25 × 25 mm for mounting on 0.4 mm-thick plastic microscope slides (Vesey Arts and Crafts, Birmingham, UK). Samples were soaked in isotonic saline (PBS 0.9%; Sigma Aldrich, St. Louis, MO, USA) for 1 min to ensure complete hydration and remove residual blood. Prior to mounting the sample, a 9.6 mm diameter hole was punched through a pair of plastic microscope slides to open a window for HIFU exposure and optical measurements. The samples were sandwiched between the slides and affixed at each end with rapid-set epoxy (Araldite Instant; Huntsman Advanced Materials, Everberg, UK) to secure the tissue. Prepared samples were wrapped in saline-moistened tissue and refrigerated at 4 °C for no longer than 8 h prior to use. Tissue samples were hydrated just prior to all HIFU exposures and optical measurements using a dropper with isotonic saline and any residual fluid was removed by blotting with a tissue (Kimwipe; Kimberly-Clark, Kent, UK). A sketch of the sample holder geometry and photograph of a mounted tissue sample is shown in figure 1.

2.2. HIFU exposure

Tissue samples were exposed to HIFU using a 1.1 MHz transducer (H-102; Sonic Concepts, Bothell, WA, USA) which was spherically focused (63 mm radius of curvature) with a 22.6 mm central opening and 64 mm outer active diameter. In order for the spectrophotometer to measure optical properties it was necessary to produce a uniform HIFU heating profile in an area of tissue at least as large as the 2 mm diameter of the light beam, which could not be achieved with this transducer due to its small focal spot size. Therefore, a low-profile lens (Ffield

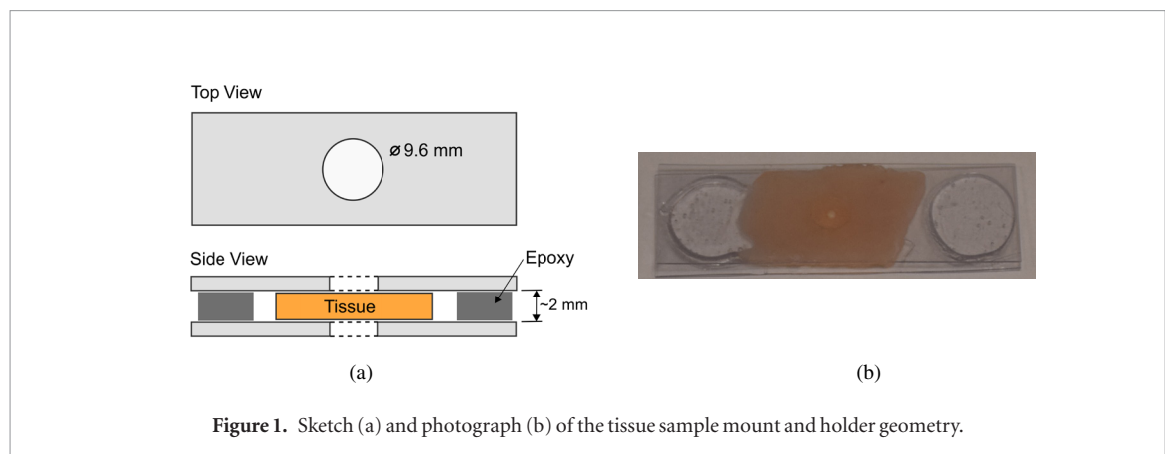


Figure 1. Sketch (a) and photograph (b) of the tissue sample mount and holder geometry.

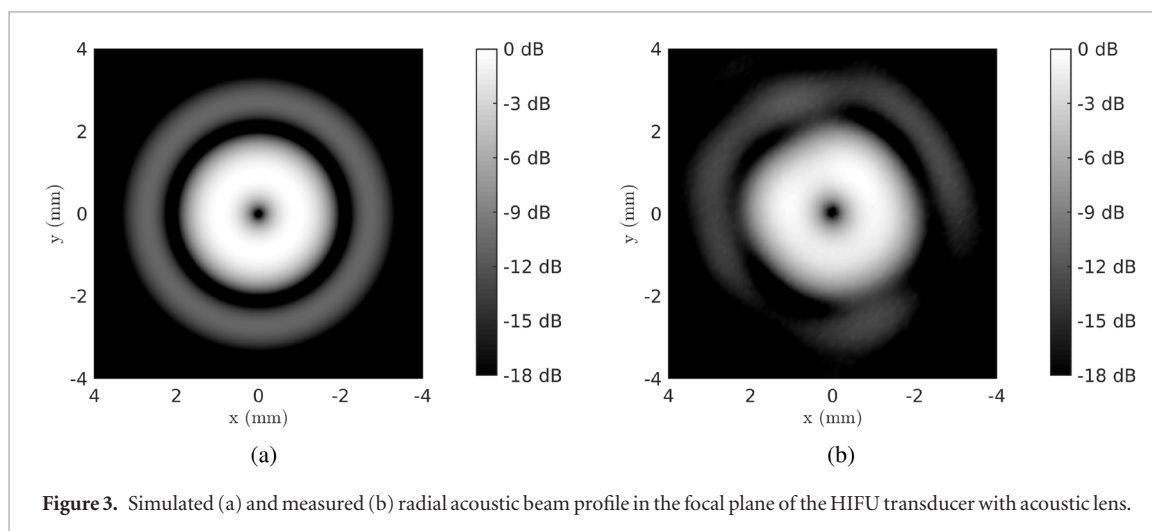
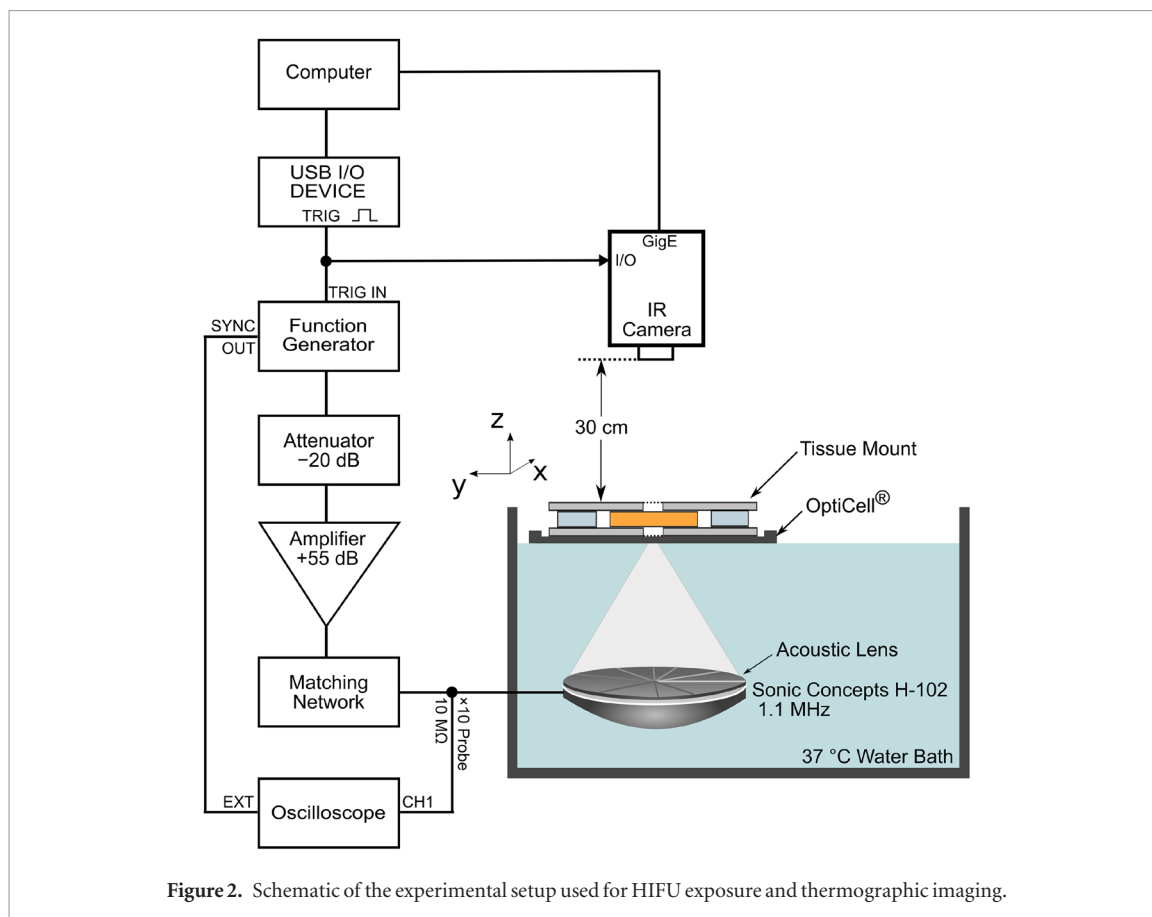
et al 1997, 1999) was used to produce a sector-vortex phase pattern (Umemura and Cain 1989) to produce a larger focal region. The lens was machined from a 6 mm thick sheet of high-impact polystyrene (CP119-06; Cut Plastic Sheeting, Ivybridge, UK) and consisted of 16 equal-area annular sectors with thickness varying in equal increments from 1.09 mm to 5.95 mm. Phase shifts produced by the lens introduced one phase rotation (0 to 2π) around the perimeter of the disk, which resulted in an annular focal zone for which the acoustic intensity maximum was located 1 mm off-axis in the geometric focal plane. The transducer was driven using a continuous-wave sinusoidal voltage provided by a signal generator (Model 39; Wavetek, San Diego, CA, USA) in series with an attenuator (-20 dB; Telegärtner, Hertfordshire, UK) and power amplifier ($+55$ dB, A150; Electronic Navigation Industries, Rochester, NY, USA). An oscilloscope (LT344; LeCroy, Chestnut Ridge, NY) was used to monitor the voltage applied to the transducer.

Experiments were performed in a tank filled with purified (Direct-Q; Millipore Ltd, Middlesex, UK) and degassed water maintained at 37°C using a circulating water heater (GD100; Grant Instruments, Cambridge, UK). The purpose of degassing was to minimize the likelihood of acoustic cavitation and spurious bubble formation on submerged surfaces. Degassing was accomplished by heating the water to at least 70°C in an aluminum vacuum chamber (Sealvac; HVACStore, Andover, UK) at atmospheric pressure. The pressure was reduced to the vapour pressure of water (~ 31 kPa at 70°C) using an aspirator pump (Eyela A-1000S; Tokyo Rikakikai Co., Tokyo, Japan) for at least 15 min during which time the water boiled rapidly as gas was continuously evacuated from the chamber. The water was left to cool at reduced pressure in the vacuum chamber overnight. The degassed water ($<5\%$ saturation at room temperature) was siphoned from the reservoir to the tank and hollow polypropylene ball bath covers (20 mm; Cole-Parmer Instrument Company, London, UK) were used to reduce in-gassing of the water during experiments. The dissolved oxygen saturation was checked periodically to ensure the bath did not exceed 60% saturation (4 mg l^{-1}) during the experiment.

The transducer and lens were mounted on a linear positioning stage (M-423; Newport Corp., Irvine, CA, USA) with the acoustic beam directed vertically upward. Mounted tissue samples were placed on an acoustically-transparent stage fashioned by removing the top membrane of a tissue culture cassette (Nunc OptiCell®; Thermo Scientific, Wiesbaden, Germany). The remaining $100\text{ }\mu\text{m}$ polystyrene film bottom membrane was used to support the tissue, and the frame was attached to a 3D translation system for positioning (M-423; Newport Corp.). The top surface of the tissue was exposed to air to permit non-contact thermal measurements using an infrared camera. A thin layer of ultrasonic coupling gel was applied between the polystyrene film and bottom surface of the tissue to provide acoustic coupling, and the bottom surface of the polystyrene film was in contact with the water bath. The polystyrene film membrane served to minimize acoustic streaming due to the HIFU field which would otherwise contribute to movement of the tissue and enhanced cooling of the bottom surface of the tissue—effects which were observed in preliminary experiments with the tissue in direct contact with the water bath. Direct contact between the tissue and the bath was also avoided to prevent changes to the tissue due to the low osmolality of the purified water bath (e.g. hydration, swelling and discoloration). The polystyrene film interface was positioned at a distance of 57.5 mm from the HIFU transducer, measured using pulse-echo time (5077PR; Panametrics NDT, Waltham, MA, USA) and was visually inspected prior to HIFU exposure to ensure no visible bubbles or trapped gas were present in order to improve coupling of the acoustic beam into the tissue. Figure 2 shows a schematic of the experimental setup for HIFU exposure and thermographic imaging.

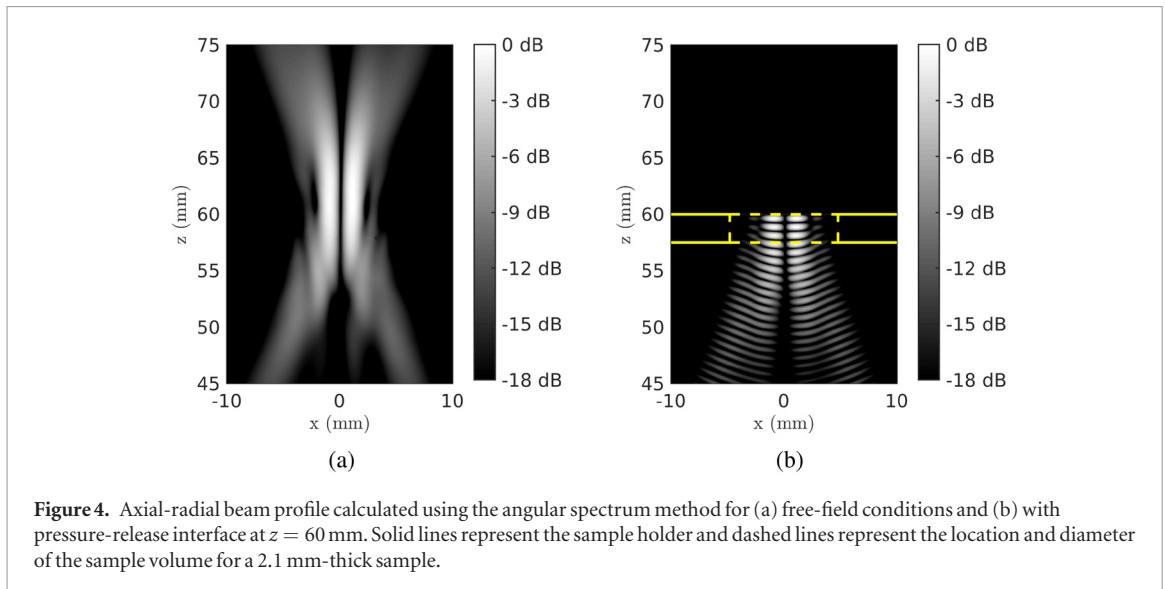
2.3. Acoustic beam profile

The HIFU transducer and lens combination was calibrated using a 0.2 mm membrane hydrophone (UT1602-068; Precision Acoustics, Dorchester, UK; sensitivity $13.4\text{ mV MPa}^{-1} \pm 6\%$). Acoustic field simulations were carried out using the Rayleigh-Sommerfeld integral (Fan and Hynynen 1992). The simulations assume linear



acoustic propagation and model the lens as a perfect phase screen; attenuation effects due to the lens were not included in the simulation. Figures 3(a) and (b) show the simulated and measured radial acoustic beam profiles near the focal plane ($z = 63$ mm) for the transducer and lens combination. The half-width of the annulus is 1.1 mm and the spacing between peaks in the radial dimension is 2 mm. The total insertion loss due to the lens was approximately 2.2 dB based on hydrophone measurements of the focal peak pressure.

Figure 4(a) shows the axial-radial beam profile calculated under free-field conditions using beam profile data measured at a distance of $z = 57.5$ mm from the lens as a source condition, and the angular spectrum method for forward and backward projection of the acoustic field (Stepanishen and Benjamin 1982). A grid spacing of $30 \mu\text{m}$ was used to project the diffractive linear acoustic field to orthogonal planes along the beam axis (Clement and Hynynen 2000). Figure 4(b) shows the beam profile calculated by reflecting the acoustic field to satisfy the pressure-release boundary condition at the interface $z = 60$ mm. This example illustrates the standing wave effect under the experimental conditions, where the pressure-release interface corresponds to the approximate location of the tissue-air interface (assuming a gap of 0.4 mm between the mylar and tissue—corresponding to the thickness of the microscope slide—and a sample thickness of 2.1 mm).



Because the acoustic field is a standing wave, the commonly employed progressive plane wave equation for heat deposition, $\langle q_v \rangle = 2\alpha I$, is not appropriate. Nyborg (1981) showed that for an arbitrary wave field the general expression for heat deposition over one cycle of a continuous wave is $q_v = \alpha p_0^2 / \rho c$ where p_0 is the spatially dependent pressure amplitude of the wave. For the case of a 1D standing wave this can be approximated as:

$$\langle q_v(z) \rangle = 4\alpha I_0 [1 - \cos(2kz)] \quad (1)$$

where I_0 is the free-field intensity of the incident acoustic wave (Myers and Giridhar 2011). The heating therefore varies from 0 to $8I_0$ as a function of distance from the reflecting surface. The mean heating is $4\alpha I_0$, which is double that of a progressive wave—this is consistent with the fact that on average the incoming wave and outgoing wave will each deposit $2\alpha I_0$.

For our experiments we require the temperature field to be uniform throughout the volume of tissue that will be interrogated optically. Therefore, we need to rely on thermal conduction to smooth out the spatial variations in the heating. A lower limit on the sonication time necessary for the thermal field to fully develop spatially can be estimated from the thermal time constant $\tau = (\lambda/2)^2 / \kappa$, where $\lambda/2 = 0.7$ mm is the standing wave periodicity and $\kappa = 0.15 \text{ mm}^2 \text{ s}^{-1}$ is the thermal diffusivity (Huang and Liu 2009, Adams *et al* 2017), and yields a value of ~ 3 s.

2.4. Infrared thermography

Infrared (IR) thermographic measurements have been used in ultrasound mediated heating to measure the influence of heating rate, diffusion, and boundary effects (Bobkova *et al* 2010, Myers and Giridhar 2011, Shaw *et al* 2011, Khokhlova *et al* 2013, Yu *et al* 2013). IR-based methods have also been used for monitoring HIFU exposures resulting in moderate temperature increase (Hsiao and Deng 2016) as well as lesion formation in *ex vivo* tissue (Hsiao *et al* 2013). Here, the surface temperature of the tissue was measured using an IR camera (A655sc; FLIR Systems, Kent, UK) with a 25° lens ($f/1.0$). The uncooled microbolometer detector is sensitive to infrared radiation of wavelengths $7.5\text{--}14 \mu\text{m}$, with a stated temperature accuracy of $\pm 2^\circ \text{C}$ and resolution of 0.03°C (14-bit dynamic range, <8 ms time constant). Conversion from radiance to temperature was performed using the calibration and non-uniformity corrections provided by the manufacturer. The IR camera was positioned 30 cm above and perpendicular to the tissue surface for imaging, as shown in figure 2. A ruler with indented gradations visible in infrared was placed on the sample stage at the approximate tissue surface plane for focus adjustment and spatial calibration prior to each experiment. The pixel size is about $220 \times 220 \mu\text{m}$ and the depth-of-field is ~ 1 cm at a range of 30 cm. Thermographic image acquisitions were synchronized with HIFU exposures using a square-wave output generated using a multifunction USB I/O device (USB-6003; National Instruments) connected in parallel with the external trigger of the camera and the external gate of the function generator. Thermographic cineloops were recorded at 640×120 pixel resolution and 50 Hz frame rate and stored to be analyzed off-line. Image analysis and computations were performed using ResearchIR software (FLIR Systems) and MATLAB (Mathworks, Natick, MA, USA).

2.5. Emissivity measurement

Accurate thermographic measurement using infrared imaging requires knowledge of the emissivity of the material. The emissivity, ϵ , is defined as the ratio of the radiation emitted by the tissue to the radiation emitted

by a blackbody radiator at the same temperature. Emissivity depends on the material and surface characteristics and scales from 0 (perfect reflector) to 1 (perfect blackbody). Estimates of the emissivity of chicken breast were obtained using the reference emissivity material method (Madding 2003, Usamentiaga *et al* 2014). Surface temperature measurements acquired on the tissue were compared with a nearby reference surface that was coated with a substance of known emissivity. Black vinyl electrical tape ($\varepsilon = 0.95$, 3M Scotch Super 33+; 3M Company, St. Paul, MN, USA) was affixed to the top surface of a thick (>1.5 cm) section of tissue which was heated from the bottom using a hot plate (Stuart US152; Bibby Scientific Limited, Stone, UK). Thermographic measurements of the black vinyl tape and the exposed chicken breast tissue were acquired every 5 s for a duration of approximately 10 min as the tissue was heated from room temperature to ~ 70 °C. The emissivity in a region of interest (ROI) centered on the tissue surface was adjusted using the built-in software *emissivity calculator* tool (ResearchIR, FLIR Systems) to yield a temperature reading that was the same as the temperature of a ROI centered on the black tape. Prior to each recording, the apparent reflected temperature detected by the camera from nearby sources was measured using a diffuse reflector (crumpled and re-flattened piece of aluminum foil) placed at the measurement location and was typically 23 °C ± 1 °C. Obtaining accurate estimates using this method requires that the target object must be heated until it reaches the temperature that will be reached under real working conditions, and the surface temperature should be at least 33 °C greater than the apparent reflected temperature (Madding 2003), therefore, emissivity values were averaged only for surface temperature exceeding 56 °C.

The emissivity of unexposed chicken breast tissue samples measured in this study was 0.75 ± 0.06 ($n = 3$). Emissivity estimates were obtained in the temperature range 57 °C– 67 °C and varied by $<5\%$ for each sample in this temperature range. Bulk heating of the tissue bottom surface using a hot plate did not result in a noticeable change of the color or texture (i.e. not thermally denatured) of the top surface during the measurement. The average emissivity value was used for conversion of IR radiance to temperature for all samples.

2.6. Thermal dose calculation

The Sapareto and Dewey (1984) model was used to calculate the thermal dose delivered to the tissue from the measured time-temperature profiles, using:

$$\text{CEM}_{43} = \sum_{t=0}^{t_f} R^{(43 - T)} \Delta t \quad (2)$$

where CEM_{43} is the thermal dose in cumulative equivalent minutes at 43 °C, T is the mean temperature during time Δt , and R is the isodose constant, taken as 0.50 above 43 °C and 0.25 below 43 °C. The thermal dose relates the time-temperature profile for any exposure to a dose in cumulative equivalent minutes at the reference temperature, 43 °C. The CEM_{43} for each pixel was calculated using equation (2) and then the average CEM_{43} for the ROI determined by calculating the geometric mean. The HIFU exposure intensity and time were varied in order to determine the optical property changes in tissue as a function of the measured thermal dose.

2.7. Spectrometer measurements

Measurements of the total transmittance and reflectance of the tissue samples were made between 400 – 1300 nm using a dual-beam UV–vis–NIR spectrometer (Lambda 750s; PerkinElmer, Beaconsfield, UK) equipped with a 100 mm integrating sphere (LabSphere Inc., North Sutton, NH, USA). Focusing lenses and an iris diaphragm were used to reduce the beam diameter for both transmittance (Transmission small spot kit, L6022023; PerkinElmer) and reflectance (Reflectance small spot kit, L6022024; PerkinElmer) measurements. The beam illuminated area on the tissue sample was approximately 2 mm in diameter for both configurations. The transmission port (11×24 mm) and reflectance port (17×22 mm) were fitted with a 10 mm diameter circular aperture for transmittance and reflectance measurements, respectively. The reference beam port of the integrating sphere was 13×25 mm and the reference beam energy was adjusted using an iris diaphragm to balance with the sample beam and decrease the dynamic range of the measurement. Measurements were recorded at 2 nm intervals in optical wavelength, using 0.40 s integration time and a slit width of 5 nm in the visible regime and servo-controlled slit width in the NIR regime, resulting in spectral bandwidth of 2 – 20 nm in this region. Both the spectrometer grating changeover and the changeover between the visible light detector (Hamamatsu R928 PMT) and NIR detector (InGaAs) of the spectrometer were set to 860.8 nm.

2.8. Optical property calculations

The measurements of total transmittance and reflectance, and the sample thickness, were used to calculate the absorption coefficient μ_a (cm^{-1}) and the reduced scattering coefficient μ'_s (cm^{-1}) using the inverse adding-doubling (IAD) algorithm (Prah *et al* 1993). The spectrometer system measures the ratio of the reference and sample beam energy, therefore eliminating the need for sphere efficiency corrections. The tissue index of refraction was assumed to be 1.4 , and the anisotropy factor was assumed to be 0.97 for the IAD calculations (Duck 1990,

Sun and Wang 2010). We also make use of the result obtained by Adams *et al* (2014) that the anisotropy factor for chicken breast did not change significantly after heating in a water bath. The effective attenuation coefficient, μ_{eff} , was calculated using the following expression, which is valid when scattering dominates absorption (Cheong *et al* 1990):

$$\mu_{\text{eff}} = \sqrt{3\mu_a(\mu_a + \mu'_s)}. \quad (3)$$

The spectrophotometer measurements and IAD inversion algorithm were validated using a 2 mm thick polyurethane optical phantom (Biomimic F0509; INO, Québec, Canada) in place of the tissue. Based on the manufacturer's data sheet, the index of refraction was taken to be 1.521 and the anisotropy factor 0.62. Good agreement was found between our measured values at 800 nm which were $\mu'_s = 10.9 \pm 0.13 \text{ cm}^{-1}$ and $\mu_a = 0.108 \pm 0.006 \text{ cm}^{-1}$ (mean \pm SD; $n = 5$) and the values provided by the manufacturer which were $\mu'_s = 10.2 \pm 0.35 \text{ cm}^{-1}$ and $\mu_a = 0.118 \pm 0.007 \text{ cm}^{-1}$ measured using a time-resolved transmittance technique (Bouchard *et al* 2010).

3. Results

3.1. Temperature rise and thermal dose delivered to tissue

Figure 5 shows the spatial surface temperature profile measured by the IR camera at 0.5 s, 1.0 s and 2.0 s for a 2.64 mm thick sample subject to a HIFU exposure at 94 W cm^{-2} . An annular heating pattern corresponding to the intensity distribution with peaks at $\pm 1 \text{ mm}$ is evident at 0.5 s exposure which fills in due to thermal conduction to yield a nominally flat temperature profile after $\sim 2 \text{ s}$ —a time scale comparable to the thermal diffusion estimate of $\sim 3 \text{ s}$. The mean and standard deviation of the temperature within the 2 mm diameter ROI was $36.1^\circ\text{C} \pm 0.2^\circ\text{C}$ at 0 s, $38.1^\circ\text{C} \pm 0.6^\circ\text{C}$ at 0.5 s, $39.9^\circ\text{C} \pm 0.7^\circ\text{C}$ at 1.0 s and $42.7^\circ\text{C} \pm 0.8^\circ\text{C}$ at 2.0 s.

Figure 6 shows the temporal evolution of the mean temperature and accumulated thermal dose within the ROI for 5 s, 10 s and 15 s exposures at 94 W cm^{-2} . The initial slope of the temperature-time curves was similar, but the peak temperature varied due to the different durations of exposure. The peak temperature (mean \pm SD within the ROI) was $49.3^\circ\text{C} \pm 1.2^\circ\text{C}$, $57.0^\circ\text{C} \pm 1.0^\circ\text{C}$, $60.8^\circ\text{C} \pm 1.5^\circ\text{C}$ and the total accumulated thermal dose (geometric mean within the ROI) was 2.28 min, 542 min, and 9350 min, respectively.

3.2. Optical properties of tissue

A total of 66 samples were analyzed, with thicknesses ranging from 1.6–3.0 mm. Samples were subjected to a 5 s, 10 s, or 15 s HIFU exposure at an intensity of 72 W cm^{-2} , 94 W cm^{-2} , 120 W cm^{-2} , or to a sham exposure in which no HIFU was applied. The sham exposure group was included to determine the optical properties of unexposed tissue. A summary of the exposure parameters, sample thickness, maximum temperature and thermal dose response is given in table 1. Figure 7 plots the accumulated thermal dose as a function of maximum temperature achieved within the tissue ROI for each sample and for the three different power settings. The range of measured maximum temperature spans from 45°C – 74°C and the range of the values of thermal dose (CEM_{43}) spans over 9 decades.

The optical properties of each sample were measured following HIFU or sham exposure. Typical raw reflectance and transmittance curves are presented in figures 8(a) and (b) for three samples exposed to different thermal doses. The samples were exposed to 94 W cm^{-2} for 5 s, 10 s and 15 s, and were of comparable thickness ($2.51 \pm 0.02 \text{ mm}$, $2.44 \pm 0.02 \text{ mm}$, and $2.44 \pm 0.02 \text{ mm}$). The maximum temperature was $T_{\text{max}} = 44.7^\circ\text{C}$, 58.8°C , and 66.5°C and the exposures resulted in an accumulated thermal dose of $\text{CEM}_{43} = 0.13 \text{ min}$, $4.3 \times 10^3 \text{ min}$, and $1.2 \times 10^6 \text{ min}$, respectively.

Figure 8(c) shows the optical reduced scattering coefficient spectra calculated as described in the Methods section. The reduced scattering coefficient varies relatively smoothly with wavelength and as thermal dose was increased it showed a consistent increase in the entire range of wavelengths investigated as a function of thermal dose. The highest scattering coefficients were measured in the near-UV range at 400 nm and decreased monotonically over the range of wavelengths investigated, reaching a minimum in the near infrared range at 1300 nm.

Figure 8(d) shows the calculated optical absorption coefficient. Two minima are observed; the strongest at about 850 nm and a second near 1100 nm, corresponding to the first and second NIR window in biological tissues, respectively (Sordillo *et al* 2014). The absorption bands at 420 nm and 550 nm correspond to oxyhemoglobin (Jacques 2013). Fatty tissues such as breast have an absorption peak near 930 nm (Jacques 2013) which is masked by the water absorption peak near 980 nm. The absorption coefficient showed appreciable increase with thermal dose in the spectral range between 600–1150 nm. The lowest absorption was measured between 800–900 nm. Below 500 nm and above 1150 nm, the absorption for all three samples was about the same ($> 1 \text{ cm}^{-1}$).

Thermal dose dependent changes were evaluated in order to determine the relationship between optical properties and thermal dose. In figure 9, the reduced scattering coefficient (μ'_s) at three optical wavelengths is plotted as a function of the total accumulated thermal dose for all exposures. In each case the data exhibited a

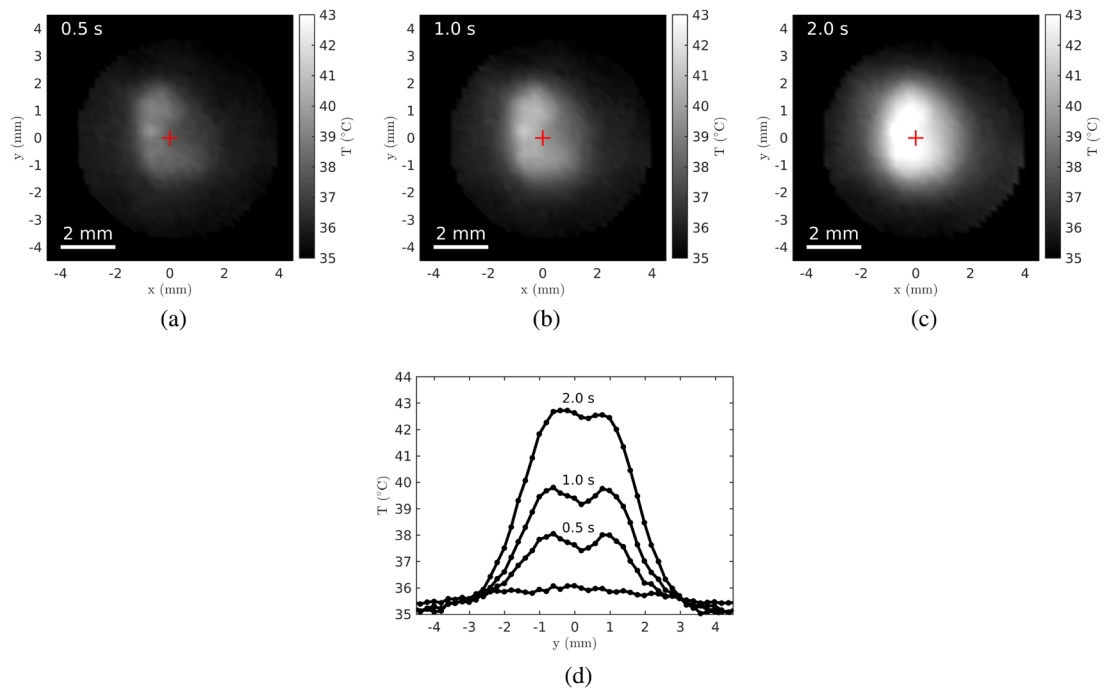


Figure 5. Surface temperature measured at (a) 0.5 s, (b) 1.0 s and (c) 2.0 s for a 94 W cm^{-2} exposure. The red crosses mark the center of the ROI. The measured radial temperature profile for the exposures is shown in (d).

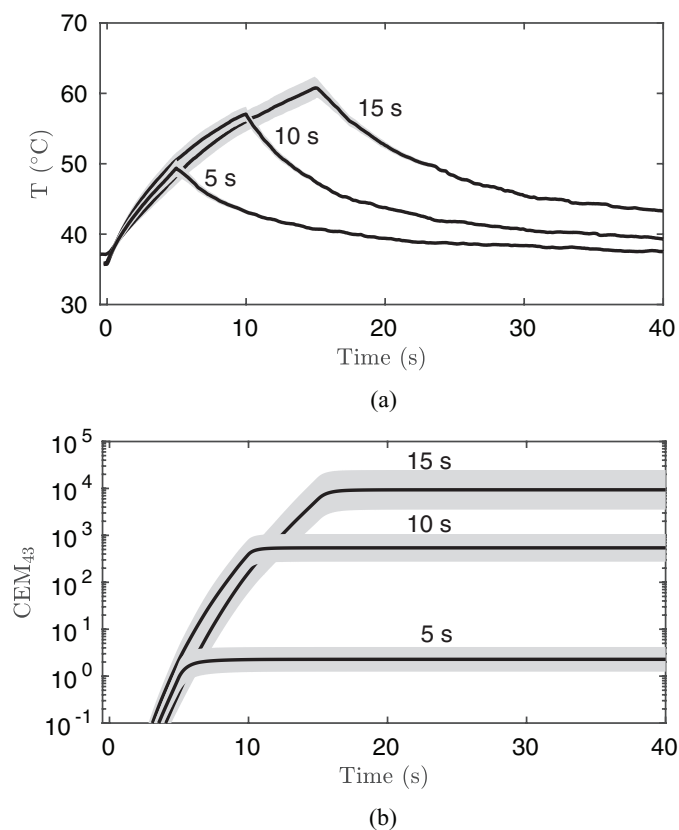


Figure 6. Temperature (a) and accumulated thermal dose (b) in the ROI for 5 s, 10 s, and 15 s exposures at 94 W cm^{-2} . The thickness of the tissue samples was 2.64 mm, 1.86 mm, and 2.41 mm, respectively. The shaded regions indicate the standard deviation of values within the ROI.

knee between 100–1000 CEM. Segmented linear regression using the least-squares method was used to fit the data and detect the transition point between the first regime, in which the slope of the fit was constrained to zero, and second regime, in which the slope of the best fit line was non-zero and therefore a change in scattering was evident as a function of the thermal dose. The coefficient of determination (R^2) was calculated to indicate

Table 1. Summary of exposure parameters for all samples.

Intensity I_0	Pressure p_{\max}	Duration	Number of samples	Thickness (mm)	Maximum temperature (°C)	Thermal dose (CEM ₄₃)
Sham exposure		n/a	8	1.94–3.00	34.1–37.2	$1.3 \times 10^{-6} - 2.9 \times 10^{-4}$
72 W cm ⁻²	3.0 MPa	10 s	6	2.09–2.66	49.8–55.0	$7.0 \times 10^0 - 1.6 \times 10^2$
		15 s	6	1.97–3.02	46.6–53.3	$1.0 \times 10^0 - 9.3 \times 10^1$
94 W cm ⁻²	3.4 MPa	5 s	6	2.26–2.97	46.2–50.8	$1.3 \times 10^{-1} - 7.0 \times 10^0$
		10 s	7	1.70–2.82	50.2–68.5	$4.0 \times 10^0 - 2.3 \times 10^5$
		15 s	9	1.65–2.97	55.2–73.4	$6.6 \times 10^1 - 1.2 \times 10^6$
120 W cm ⁻²	3.8 MPa	5 s	8	1.75–2.64	45.0–52.5	$1.8 \times 10^{-1} - 2.2 \times 10^1$
		10 s	7	1.60–2.63	58.6–76.5	$9.3 \times 10^2 - 3.1 \times 10^7$
		15 s	7	1.64–2.34	60.7–79.6	$2.5 \times 10^3 - 2.4 \times 10^8$

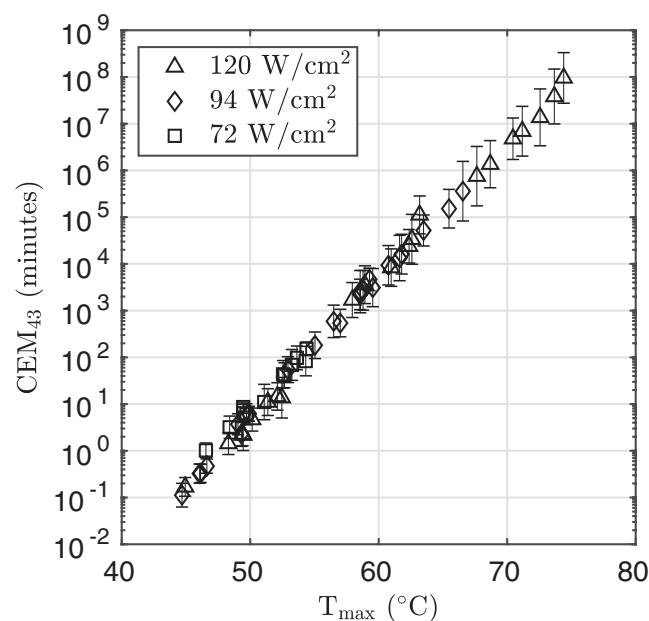


Figure 7. Measured maximum temperature and thermal dose in the ROI for all exposures. Error bars indicate the standard deviation of the log-normally distributed thermal dose within the ROI. For sham treatments (not shown, $n = 11$) the average temperature was $T_{\max} = 35.2^\circ\text{C} \pm 1.4^\circ\text{C}$ and thermal dose ranged from $\text{CEM}_{43} = 1.3 \times 10^{-6}$ min to 2.9×10^{-4} min.

the goodness of fit, yielding 0.82, 0.83, and 0.84 for the fits at 532 nm, 850 nm, and 1064 nm, respectively. Taking the point where the best fit lines in each regime intersect yields an estimate for the threshold value $\text{CEM}_{43}^{\text{thres}}$. The threshold thermal dose and slope of the best-fit line characterizing the change in scattering of tissue was evaluated for all wavelengths and the result is shown in figure 10. The minimum threshold value of 222 min occurs at 406 nm and for $\lambda > 430$ nm the threshold was 600 ± 81 min (mean \pm standard deviation).

Figure 11 shows the equivalent data for absorption. In this case there was not a clear breakpoint in the data with CEM_{43} and attempting to fit the data in a similar manner resulted in $R^2 < 0.2$, indicating that the assumption of two regimes with a transition point was not supported. At some wavelengths there appears to be increase in absorption versus thermal dose but the variability in the data is too large to determine a threshold.

In figure 12 the reduced scattering coefficient (μ'_s), absorption coefficient (μ_a), and effective attenuation coefficient (μ_{eff}) are presented for all exposures grouped as follows: (i) sham, (ii) exposures for which the thermal dose fell below the scattering-based threshold value, (iii) exposures for which the thermal dose fell above the scattering-based threshold with $T_{\max} < 70^\circ\text{C}$ and (iv) exposures for which the thermal dose fell above the scattering-based threshold with $T_{\max} > 70^\circ\text{C}$. The reduced scattering and absorption for selected wavelengths are given in table 2. A two-sample t -test was performed to indicate if the differences between groups was statistically significant ($p < 0.05$). Differences between the sham exposures (group i) and the below-threshold exposures (group ii) were not significant (not shown). Differences between group i and group iii were significant, except for

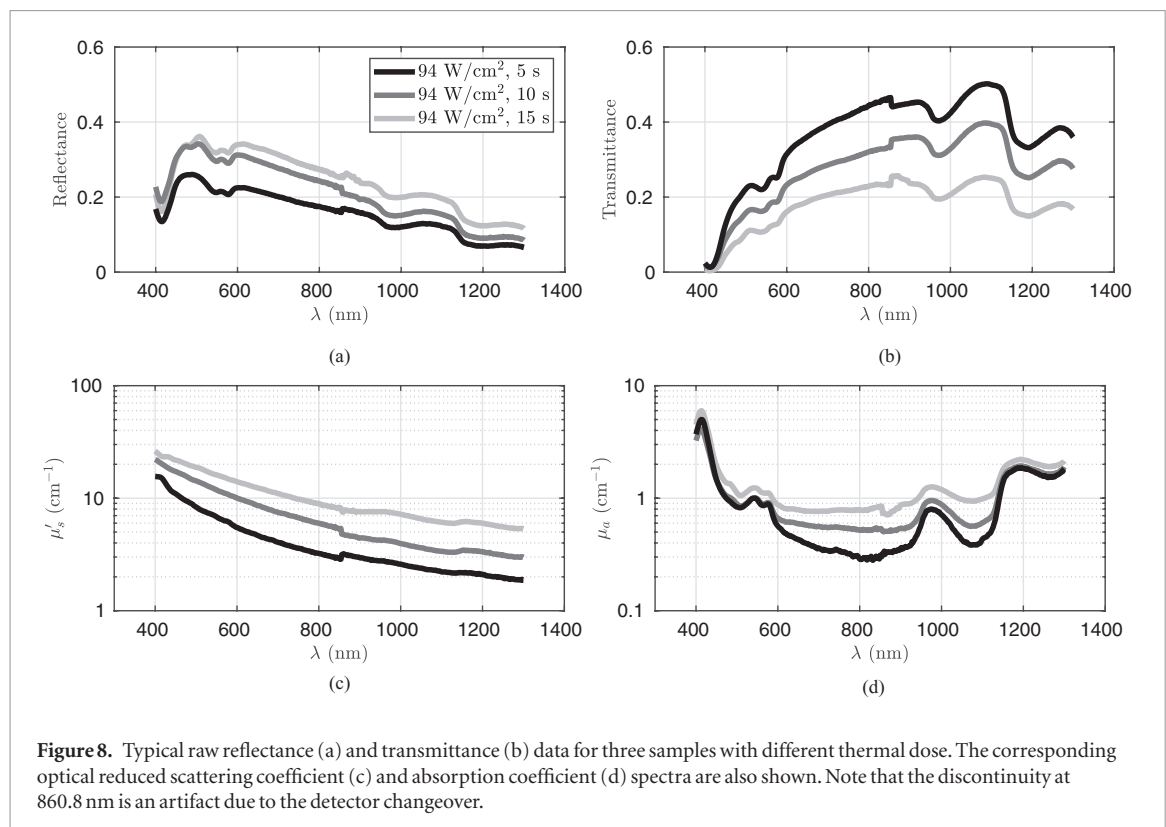


Figure 8. Typical raw reflectance (a) and transmittance (b) data for three samples with different thermal dose. The corresponding optical reduced scattering coefficient (c) and absorption coefficient (d) spectra are also shown. Note that the discontinuity at 860.8 nm is an artifact due to the detector changeover.

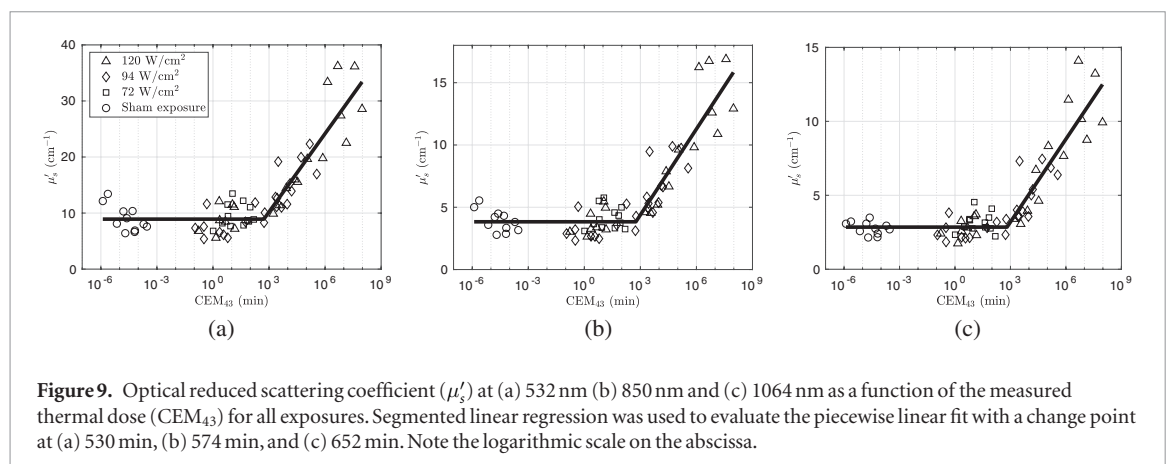


Figure 9. Optical reduced scattering coefficient (μ'_s) at (a) 532 nm (b) 850 nm and (c) 1064 nm as a function of the measured thermal dose (CEM_{43}) for all exposures. Segmented linear regression was used to evaluate the piecewise linear fit with a change point at (a) 530 min, (b) 574 min, and (c) 652 min. Note the logarithmic scale on the abscissa.

the value of the absorption coefficient at 532 nm. Differences between group iii and group iv were significant for the reduced scattering coefficient and the effective attenuation coefficient, but not for the absorption coefficient.

4. Discussion

The intensity and exposure time combinations used in this study allowed us to achieve temperature rises and thermal doses due to HIFU exposure that were clinically relevant. In order to generate a large enough volume of tissue subject to uniform heating to measure the optical properties a sector-vortex lens was employed so that the temperature was nearly constant within a central 2 mm diameter area. The surface temperature of the tissue was monitored with an IR camera in order to calculate the thermal dose based on real-time thermometry. The maximum temperature rise was 45 °C–74 °C, the insonation times were 5–15 s and the range of thermal dose (CEM_{43}) was 10⁻¹–10⁹ min.

The optical properties for chicken breast that were not exposed to HIFU were $\mu'_s = 6.45 \pm 1.65$ cm⁻¹ and $\mu_a = 0.51 \pm 0.11$ cm⁻¹ at 630 nm and are compared with values reported in the literature in table 3. The variations found here are typical of optical properties reported in the literature, however, some comments are necessary given the wide range of reported values for the optical absorption coefficient. The integrating sphere spectrophotometric technique used here was also used in two previous studies. Adams *et al* used 2 mm thick samples and reported $\mu_a < 0.05$ cm⁻¹, but noted that this value may be unrealistic due to limitations in the system

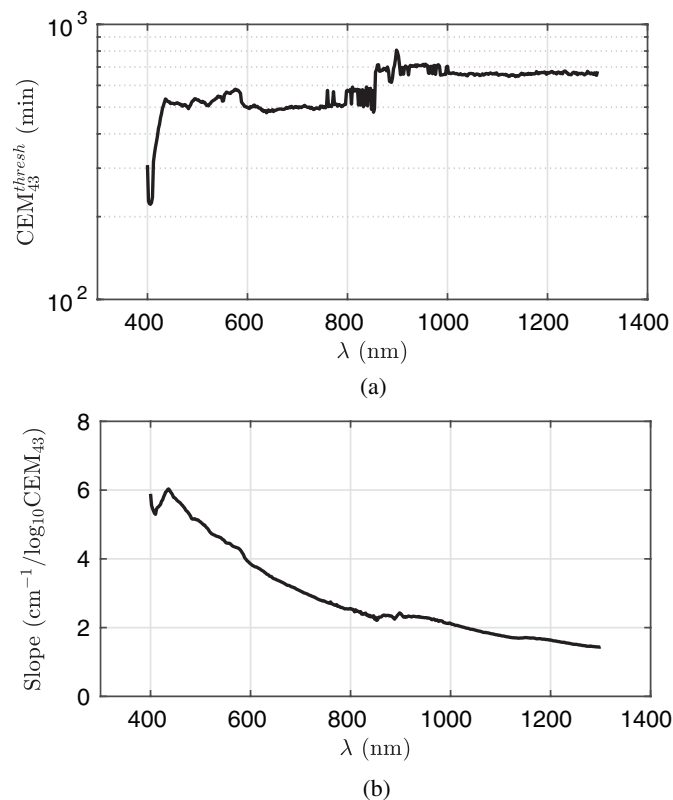


Figure 10. Threshold thermal dose value corresponding to a change in optical reduced scattering coefficient, μ'_s , versus optical wavelength, λ (a) and slope of the best-fit line in the region above the threshold value versus the logarithm (base 10) of the thermal dose (b). The intercept and slope were determined using the method illustrated in figure 9.

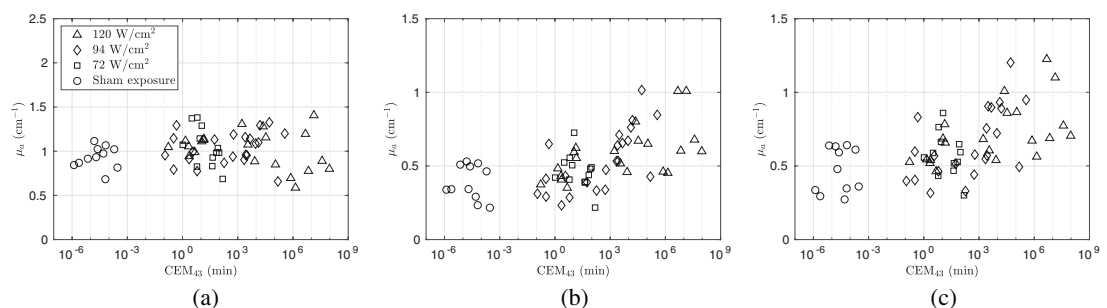
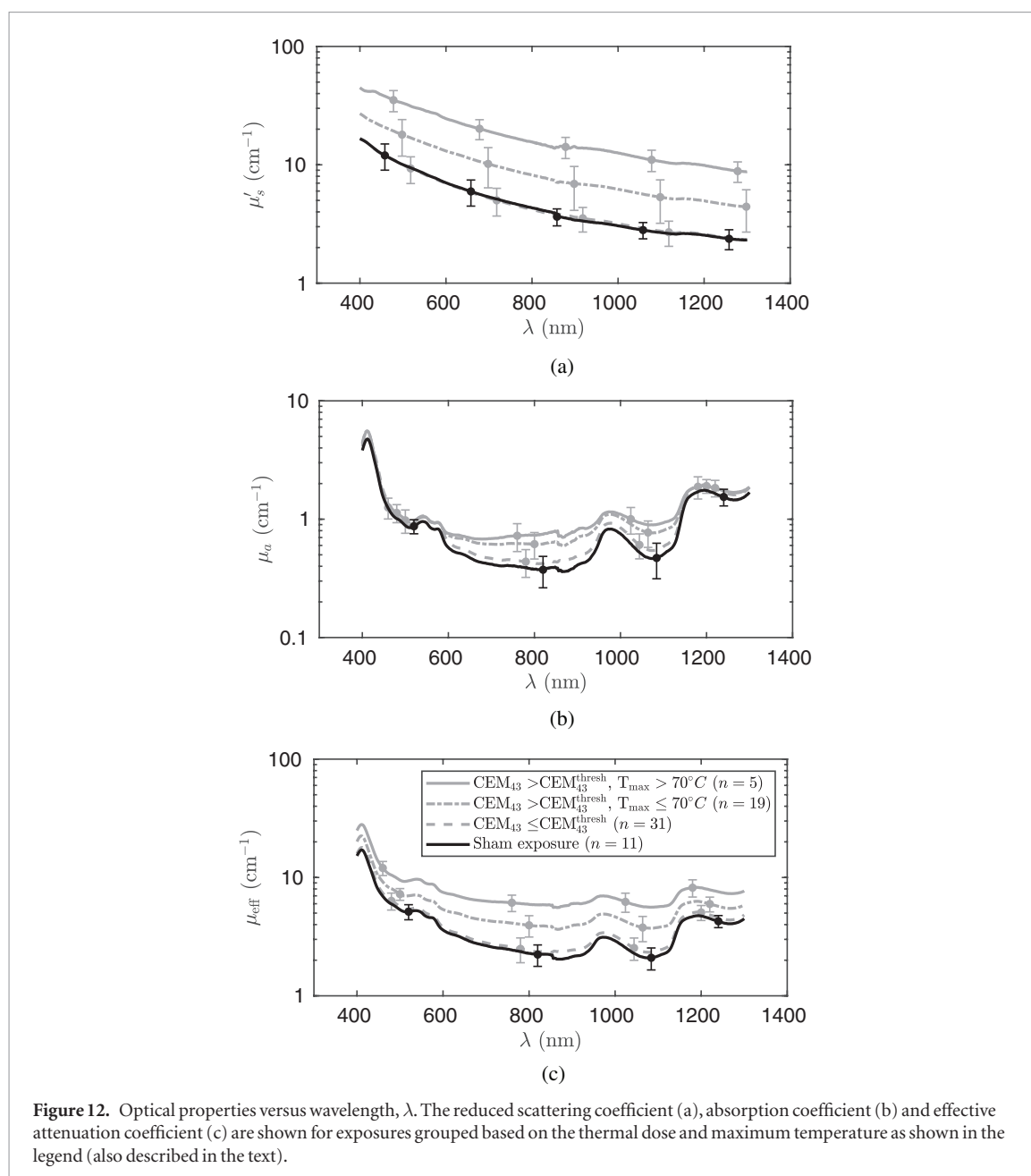


Figure 11. Optical absorption coefficient (μ_a) at (a) 532 nm, (b) 850 nm, and (c) 1064 nm as a function of the measured thermal dose (CEM_{43}) for all exposures.

when absorption is less than 0.05 cm^{-1} (Adams *et al* 2014). Alhamami *et al* (2014) reported $\mu_a = 1.2 \text{ cm}^{-1}$ using 1 mm thick samples. Our value $\mu_a = 0.51 \pm 0.12 \text{ cm}^{-1}$ lies between these previous reports. It has been suggested that for tissues with low absorption coefficient ($< 1 \text{ cm}^{-1}$), the spectrophotometric technique may be subject to error in the estimation of absorption coefficient due to measurement bias associated with small light losses during the measurement of transmittance and reflectance (Prahl *et al* 1993, Torres *et al* 1994). Torres (1994) measured values with a spectrometer that were 4 to 5 times higher than predicted for human aorta samples and noted that the primary reason absorption may be overestimated using spectrophotometric techniques is due to lost light. To estimate the magnitude of this effect in our system, we measured the properties of a 2 mm thick polyurethane phantom with known optical properties similar to those of tissue and obtained a measured value of $\mu_a = 0.108 \text{ cm}^{-1}$ at 800 nm, which was within 10% of the manufacturers' value obtained using a time-resolved technique ($\mu_a = 0.118 \text{ cm}^{-1}$; INO, National Optics Institute, Quebec, Canada).

4.1. Optical properties of tissue exposed to HIFU

The reduced scattering coefficient remained constant for CEM_{43} below a threshold. Once the thermal dose had exceeded a threshold there was a linear increase in reduced scattering with thermal dose across all optical wavelengths. The values for the reduced scattering coefficient of lesioned tissue measured in this study are in



reasonable agreement with the values reported by Adams *et al* (2014, 2017) who reported steady-state asymptotic values of $\mu'_s = 8.635 \text{ cm}^{-1}$ for $T < 70^\circ\text{C}$ and $\mu'_s = 12.76 \text{ cm}^{-1}$ if $T > 70^\circ\text{C}$ at 1064 nm. For the exposures that exceeded the apparent threshold $\text{CEM}_{43}^{\text{thresh}}$ in this study, those that reached a $T_{\text{max}} < 70^\circ\text{C}$ had a value of $\mu'_s = 5.59 \pm 2.22 \text{ cm}^{-1}$ ($n = 19$) and those that exceeded $T_{\text{max}} > 70^\circ\text{C}$ had a value of $\mu'_s = 11.23 \pm 2.30 \text{ cm}^{-1}$ ($n = 5$) (table 2). Furthermore, the greater than two-fold increase in μ'_s for tissue resulting from thermal coagulation is consistent with reports by other investigators for chicken breast (Alhamami *et al* 2014, Nagarajan and Yu 2016) as well as other tissue types (Jacques and Gaeni 1989, Agah *et al* 1996, Ritz *et al* 2001, Khokhlova *et al* 2006, Zhao *et al* 2018). These data indicate that optical scattering is a good proxy for thermal damage.

The optical absorption coefficient measurements displayed a much higher variance and there was not a clear threshold in the absorption with CEM_{43} as was observed with the scattering coefficient. The value of the absorption coefficient measured for thermally damaged tissue that exceeded $T_{\text{max}} > 70^\circ\text{C}$ was $\mu_a = 0.72 \pm 0.18 \text{ cm}^{-1}$ at 630 nm, and $\mu_a = 0.78 \pm 0.21 \text{ cm}^{-1}$ at 850 nm, about 40% and 100% higher than for unexposed tissue, respectively. The values for exposures in which $T_{\text{max}} < 70^\circ\text{C}$ were also higher than for unexposed tissue but to a lesser extent, although no significant differences were observed between exposures in which $T_{\text{max}} < 70^\circ\text{C}$ and $T_{\text{max}} > 70^\circ\text{C}$ (figure 12(b), table 2). This is consistent with the changes observed by Adams *et al* (2014) who reported asymptotic values for absorption coefficients about 2-fold higher for thermally damaged tissue than for unexposed tissue, but did not observe a threshold effect between 60°C – 70°C . We observed that the optical absorption coefficient did increase for thermally damaged tissue (figure 12(b)) although we could not determine

Table 2. Optical properties of unexposed and HIFU-exposed thermally damaged chicken breast tissue at selected wavelengths. Differences were statistically significant ($p < 0.05$) except were indicated.

CEM ₄₃ > CEM ₄₃ ^{thres}					
λ (nm)	Unexposed μ'_s (cm ⁻¹)	$T_{\max} < 70$ °C		$T_{\max} > 70$ °C	
		μ'_s (cm ⁻¹)	% change	μ'_s (cm ⁻¹)	% change
532	9.00 ± 2.31	16.15 ± 5.53	+80%	30.17 ± 5.94	+235%
630	6.45 ± 1.65	12.14 ± 4.44	+88%	22.69 ± 4.38	+252%
850	3.92 ± 0.88	7.43 ± 2.92	+89%	14.01 ± 2.68	+257%
1064	2.78 ± 0.43	5.59 ± 2.22	+101%	11.23 ± 2.30	+304%

CEM ₄₃ > CEM ₄₃ ^{thres}					
λ (nm)	Unexposed μ_a (cm ⁻¹)	$T_{\max} < 70$ °C		$T_{\max} > 70$ °C	
		μ_a (cm ⁻¹)	% change	μ_a (cm ⁻¹)	% change
532	0.93 ± 0.13	1.03 ± 0.22 ^a	+11 %	1.01 ± 0.28 ^a	+9 %
630	0.51 ± 0.11	0.69 ± 0.16	+35 %	0.72 ± 0.18 ^a	+42 %
850	0.39 ± 0.12	0.64 ± 0.16	+65 %	0.78 ± 0.21 ^a	+100 %
1064	0.47 ± 0.15	0.77 ± 0.19	+63 %	0.90 ± 0.25 ^a	+90 %

CEM ₄₃ > CEM ₄₃ ^{thres}					
λ (nm)	Unexposed μ_{eff} (cm ⁻¹)	$T_{\max} < 70$ °C		$T_{\max} > 70$ °C	
		μ_{eff} (cm ⁻¹)	% change	μ_{eff} (cm ⁻¹)	% change
532	5.23 ± 0.72	7.10 ± 0.83	+36%	9.61 ± 1.41	+84%
630	3.24 ± 0.61	5.01 ± 0.80	+55%	7.05 ± 0.96	+117%
850	2.22 ± 0.46	3.87 ± 0.82	+74%	5.82 ± 1.00	+162%
1064	2.13 ± 0.44	3.78 ± 0.91	+78%	5.67 ± 1.13	+167%

^a Not statistically significant ($p \geq 0.05$).**Table 3.** Optical properties of unexposed chicken breast tissue at 630 nm compared with values reported in the literature.

Reference	Method	Wavelength (nm)	μ'_s (cm ⁻¹)	μ_a (cm ⁻¹)
Present study	Integrating sphere	630	6.45 ± 1.65	0.51 ± 0.11
Cheong <i>et al</i> (1990)	Various	633	[3.3–8.0]	[0.12–0.17]
Kienle <i>et al</i> (1996)	Spatially-resolved diffuse reflectance	633	4.2 ± 0.5	0.038 ± 0.008
Marquez <i>et al</i> (1998)	Oblique incidence reflectometry	630	[2.4–2.7]	[0.05–0.20]
Adams <i>et al</i> (2014)	Integrating sphere	630	2.2	<0.05
Alhamami <i>et al</i> (2014)	Integrating sphere	630	4	1.2
Nagarajan and Yu (2016)	Spectral diffuse reflectance	430–630	2.69 ± 0.08	0.29 ± 0.01

a threshold for this effect with respect to the thermal dose. The presence of chromophores in the tissue will have a notable effect on the optical absorption and variability in color between tissue samples will affect the absorption coefficient more than the scattering coefficient. We found that the largest changes in absorption occurred in the regions immediately above and below the first water absorption band at 980 nm.

Our results for the change in optical properties for tissues exposed to thermal damage are consistent with reports by other investigators for other tissue types. For example, Jacques and Gaeeni (1989) reported an approximately 7-fold increase in μ'_s and a slight elevation in μ_a for canine myocardium achieved by coagulation at temperatures above 65 °C by immersion in water bath (594–633 nm). Khokhlova *et al* (2006) reported an approximate 2-fold increase in scattering and absorption between raw and boiled porcine liver tissue. Using a hot plate, Nagarajan and Yu (2016) reported that μ'_s for porcine muscle (430–630 nm) increased approximately 6-fold between 49 and 67 °C, and observed changes in the absorption coefficient of about 25% in the same range.

The changes observed here seem to be more pronounced at the longer wavelengths. In the UV range $\lambda < 550$ nm, absorption is high and dominated by the spectrum of hemoglobin (Jacques 2013), which would mask changes resulting from alterations in the morphology of the tissue. Changes in absorption become more

important in the visible and extending to the NIR range. Quantitatively, it is found that changes in absorption are most observable immediately above and below the first water absorption peak.

4.2. Threshold for change in optical properties due to HIFU-induced thermal ablation

The most widely employed threshold for thermal ablation treatments using HIFU is CEM_{43} of 240 min (Sinden and ter Haar 2014) but this value varies depending on tissue type. Graham *et al* (1999) used MR thermometry and post-heating MR images to quantitate HIFU thermal coagulation and found the threshold thermal dose to be in the range $CEM_{43} = 100\text{--}1000$ min in bovine kidney and liver (Graham *et al* 1999) which is consistent with our threshold of $CEM_{43} = 600 \pm 81$ min. A meta-analysis of the effect of the CEM_{43} thermal dose metric on a variety of tissues found that if the temperature exceeds 45 °C then a thermal dose of greater than 100 min is needed to induce thermal damage (van Rhooen *et al* 2013). Our data is therefore consistent with other reports that suggest a fixed value of 240 min may not be a robust indicator of thermal damage.

4.3. Tissue effects due to HIFU heating

The effect of HIFU-induced changes in tissue properties is significant because any increase in the absorption and/or reduced scattering coefficient serves to increase the attenuation coefficient and thus limits light penetration in lesioned tissue. The greater than 2-fold increase in the reduced scattering coefficient is most likely influenced by morphological damage in the tissue. For HIFU exposures exceeding $CEM_{43} = 100\text{--}1000$ min, a lesion will be generated—the tissue becomes more opaque and appears whiter. We observed that quantitative changes to the tissue scattering coefficient were detectable above a certain threshold thermal dose. We observed that changes in the reduced scattering coefficient for tissues in which $T_{\max} > 70$ °C were greater than for tissues with $T_{\max} < 70$ °C. Proteins in the tissue undergo structural changes when heated to between 60 °C and 80 °C (Nilsson *et al* 1998) which may account for this effect. More dramatic changes to the tissue microstructure may occur at higher pressure amplitudes, such as are used in histotripsy (Lundt *et al* 2017).

The increase in absorption at longer wavelengths indicates a change in the distribution and/or concentration of absorbers. Shrinkage of tissue may lead to a higher absorption coefficient, as it increases the concentration of absorbers per unit volume. It has also been proposed that changes to the structure of myofilaments in skeletal muscle, which are constructed of the proteins myosin and actin, may affect the optical properties of chicken breast (Kong *et al* 2008, Nagarajan and Yu 2016). The increase in absorption is also important for PA imaging, as an increase in absorption will lead to elevated PA signal amplitudes (Alhamami *et al* 2014).

4.4. Clinical implications

A primary limitation of widespread adoption of noninvasive HIFU therapy is the lack of low-cost and real-time monitoring and imaging techniques that can help guide the ablative therapy. These data motivate further research into the use of light-and-sound modalities to monitor HIFU therapy through changes in optical properties. For example, the greatest changes in optical absorption after lesion formation were observed at 800 nm and 1100 nm, suggesting that these would be appropriate wavelengths in which to use PA as a monitoring modality. Acousto-optic techniques, on the other hand, are sensitive to changes in both absorption and scattering and the changes in scattering were relatively insensitive to optical wavelength. Previous analysis of penetration depth for an acousto-optic system (Adams 2015) suggests that the depth at which AO can detect HIFU lesions is dependent on sensor geometry, wavelength, lesion volume, and tissue type. For example, in breast detection to 50 mm is feasible, for prostate up to 25 mm, but for liver detection is likely not possible.

We note that in lesion formation both absorption and scattering increased which will result in decreased optical penetration depth. For single lesions the impact is probably minimal, however, HIFU therapy applications typically require multiple lesions. In such cases, the relative orientation of the HIFU source and the optical transducers could substantially impact detectability (Adams *et al* 2017). We further note that this *ex vivo* study does not permit an evaluation of the changes in optical parameters induced by blood circulation.

4.5. Limitations

4.5.1. IR temperature measurement

Measurement of the temperature using an IR camera offers good spatial and temporal resolution, however, it is only possible to measure the temperature at the tissue surface. Due to the pressure-release acoustic boundary condition at the tissue-air surface, the maximum heating occurs $\lambda/4 = 0.35$ mm below the surface at the first pressure antinode. The standing wave effect produced by the reflection results in corrugation of the heating profile corresponding to the antinodes along the beam axis spaced $\lambda/2 = 0.7$ mm in the axial dimension (figure 4). Myers and Giridhar (2011) found that an exposure time of at least 1.5 s is recommended to ensure that the measured interface temperature is within 10% of the maximum temperature within the tissue and convective heat transfer may become important for longer exposure times (>2 s). In this study, a lens was used to broaden the beam to produce a larger heating profile in the radial dimension. Heat conduction in the tissue layer helps to

fill in the gaps (figure 5). Nevertheless, these factors as well as variations in the tissue result in different heating rates and imply that our measured values represent a lower bound to the actual temperature and thermal dose delivered to the tissue. However, given the huge scale of thermal dose, the variations in temperature measured on the surface of the tissue (figure 7) are reasonable to characterize the exposure.

4.5.2. Variation in emissivity and baseline optical properties of tissue

The average emissivity value measured for chicken breast tissue was used in this study for conversion from IR radiance to temperature. The emissivity of individual specimens could vary due to variations in the tissue color and may change dynamically during the exposure due to blanching of the tissue caused by HIFU-induced thermal lesions appearing on the surface. The uncertainty in temperature calculated by assuming a difference corresponding to one standard deviation in the emissivity value (Corwin and Rodenburgh 1994) would result in a discrepancy of $\pm 1.85\%$ in the temperature measurement, which is comparable to the manufacturer's stated accuracy of $\pm 2\%$ of the reading. In this study, only the final values of the optical properties were measured for each sample, so it was not possible to normalize the changes in optical scattering and absorption coefficients by their values prior to HIFU-exposure to obtain the magnitude change, although this would be a suggestion for improving future experiments.

4.5.3. Optical properties calculation and inversion

The index of refraction for tissue is taken to be 1.4 for the IAD inversion but ranges from 1.33–1.45 (Jacques 2013). The value of the tissue anisotropy is approximate and assumed to be 0.97, although this has little effect on the estimation of the reduced scattering coefficient. Photons scattered out the side of the tissue slab were considered in the IAD algorithm (Prahl *et al* 1993), however, unaccounted light losses may contribute to errors in this and other studies. It has been noted that even small light losses (for example, through the sides of the tissue sample) can produce large errors in the estimation of the absorption coefficient (Çilesiz and Welch 1993, Torres *et al* 1994). Lost light was minimized by ensuring good optical contact between the sample and the sphere and by using a plastic sample holder rather than sandwiching the sample between glass slides, however, the drawback with this method is that the result has more dependence on the surface roughness; the tissue surface is not optically flat and fresnel reflection results in some transmission loss through the sample.

4.5.4. Dehydration

Variations in the water content may affect absorption, especially for longer wavelengths (>900 nm) where water dominates the absorption spectrum. Thin tissue sections are subject to desiccation (Çilesiz and Welch 1993), however, we were careful to hydrate the tissue prior to all measurements to minimize this effect.

4.5.5. Cavitation

The maximum temperature was about 75 °C, well below the boiling temperature, and there were no events that substantially changed the heating profile (see Hsiao *et al* (2013) for examples of heating curves in which cavity formation is apparent). Although micro cavitation may contribute to an enhanced heating effect (Holt and Roy 2001), this effect would result in a measurable temperature increase and would thus be included in the thermal dose calculation.

5. Conclusions

The data obtained here comprise the first study of optical properties in chicken breast tissue over a wide range of optical wavelengths under the effect of HIFU-induced thermal coagulation. It was found that HIFU-induced thermal coagulation leads to an increase in optical scattering and absorption of chicken breast tissue. Optical scattering exhibited a clear threshold across all the optical wavelengths studied which is broadly consistent with other studies of the thermal dose threshold for lesion formation. The increase in absorption was not as marked and also showed greater dependence on wavelength. These optical property changes suggest that AO and PA sensing of lesion formation during HIFU therapy may be feasible. The greatest optical penetration depth can be found within the NIR windows near 900 nm and 1100 nm. In this range, the scattering and absorption coefficients in lesioned chicken breast tissue are 250% and 100% higher, respectively, than for unexposed tissue.

Acknowledgments

The authors gratefully acknowledge Eleanor O'Hara for technical contributions in the early stages of this work, Prof David Howey for loaning the IR camera, and the technical staff of the Physics Department machine shop for manufacturing the acoustic lens. JLR acknowledges support from the F V Hunt Postdoctoral Research Fellowship of the Acoustical Society of America. Work supported in part by the University of Oxford Department

of Engineering Science and the EPSRC, UK (Grant no. EP/K02020X/1). Supporting data are available through the Oxford University Research Archive data repository.

ORCID iDs

Jason L Raymond  <https://orcid.org/0000-0002-6367-9431>

References

- Abbass M A, Killin J K, Mahalingam N, Hooi F M, Barthe P G and Mast T D 2018 Real-time spatiotemporal control of high-intensity focused ultrasound thermal ablation using echo decorrelation imaging in *ex vivo* bovine liver *Ultrasound Med. Biol.* **44** 199–213
- Adams M T 2015 A modeling-based assessment of acousto-optic sensing for monitoring high-intensity focused ultrasound lesion formation *PhD Dissertation* Boston University, Boston, MA, USA
- Adams M T, Cleveland R O and Roy R A 2017 Modeling-based design and assessment of an acousto-optic guided high-intensity focused ultrasound system *J. Biomed. Opt.* **22** 017001
- Adams M T, Wang Q, Cleveland R O and Roy R A 2014 Thermal dose dependent optical property changes of *ex vivo* chicken breast tissues between 500 and 1100 nm *Phys. Med. Biol.* **59** 3249–60
- Agah R, Gandjbakhche A H, Motamedi M, Nossal R and Bonner R F 1996 Dynamics of temperature dependent optical properties of tissue: dependence on thermally induced alteration *IEEE Trans. Biomed. Eng.* **43** 839–46
- Alhamami M, Kolios M C and Tavakkoli J 2014 Photoacoustic detection and optical spectroscopy of high-intensity focused ultrasound-induced thermal lesions in biologic tissue: photoacoustic detection and optical spectroscopy of HIFU lesions *Med. Phys.* **41** 053502
- Bing K F, Rouze N C, Palmeri M L, Rotemberg V M and Nightingale K R 2011 Combined ultrasonic thermal ablation with interleaved ARFI image monitoring using a single diagnostic curvilinear array: a feasibility study *Ultrasonic Imaging* **33** 217–32
- Bobkova S, Gavrilov L, Khokhlova V, Shaw A and Hand J 2010 Focusing of high-intensity ultrasound through the rib cage using a therapeutic random phased array *Ultrasound Med. Biol.* **36** 888–906
- Bouchard J-P, Veilleux I, Jedidi R, Noiseux I, Fortin M and Mermut O 2010 Reference optical phantoms for diffuse optical spectroscopy part 1—error analysis of a time resolved transmittance characterization method *Opt. Express* **18** 11495
- Chen J, Li Y, Wang Z, McCulloch P, Hu L, Chen W, Liu G, Li J, Lang J and Committee of the Clinical Trial of HIFU Versus Surgical Treatment for Fibroids 2017 Evaluation of HIFU ablation for uterine fibroids: an IDEAL prospective exploration study *BJOG* **125** 354–64
- Cheong W-F, Prah S A and Welch A J 1990 A review of the optical properties of biological tissues *IEEE J. Quantum Electron.* **26** 2166–85
- Çilesiz I F and Welch A J 1993 Light dosimetry: effects of dehydration and thermal damage on the optical properties of the human aorta *Appl. Opt.* **32** 477
- Clement G T and Hynynen K 2000 Field characterization of therapeutic ultrasound phased arrays through forward and backward planar projection *J. Acoust. Soc. Am.* **108** 441–6
- Corwin R R and Rodenburgh A 1994 Temperature error in radiation thermometry caused by emissivity and reflectance measurement error *Appl. Opt.* **33** 1950
- Cui H and Yang X 2011 Real-time monitoring of high-intensity focused ultrasound ablations with photoacoustic technique: an *in vitro* study: real-time monitoring HIFU with PAI *Med. Phys.* **38** 5345–50
- Duck F A 1990 *Physical Properties of Tissue: a Comprehensive Reference Book* (London: Academic)
- Fan X and Hynynen K 1992 The effect of wave reflection and refraction at soft tissue interfaces during ultrasound hyperthermia treatments *J. Acoust. Soc. Am.* **91** 1727–36
- Fjfield T, Silcox C E and Hynynen K 1999 Low-profile lenses for ultrasound surgery *Phys. Med. Biol.* **44** 1803–13
- Fjfield T, Sorrentino V, Cline H and Hynynen K 1997 Design and experimental verification of thin acoustic lenses for the coagulation of large tissue volumes *Phys. Med. Biol.* **42** 2341–54
- Fosnight T R *et al* 2017 Echo decorrelation imaging of rabbit liver and VX2 tumor during *in vivo* ultrasound ablation *Ultrasound Med. Biol.* **43** 176–86
- Frenkel V (ed) 2010 *Therapeutic Ultrasound: Mechanisms to Applications* (Hauppauge: Nova Science Publishers)
- Graham S J, Chen L, Leitch M, Peters R D, Bronskill M J, Foster F S, Henkelman R M and Plewes D B 1999 Quantifying tissue damage due to focused ultrasound heating observed by MRI *Magn. Reson. Med.* **41** 321–8
- Gray J P, Dana N, Dextraze K L, Maier F, Emelianov S and Bouchard R R 2016 Multi-wavelength photoacoustic visualization of high intensity focused ultrasound lesions *Ultrasonic Imaging* **38** 96–112
- Han Y, Wang S, Payen T and Konofagou E 2017 Fast lesion mapping during HIFU treatment using harmonic motion imaging guided focused ultrasound (HMIgFUS) *in vitro* and *in vivo* *Phys. Med. Biol.* **62** 3111–23
- Holt R G and Roy R A 2001 Measurements of bubble-enhanced heating from focused, MHz-frequency ultrasound in a tissue-mimicking material *Ultrasound Med. Biol.* **27** 1399–412
- Hsiao Y-H, Kuo S-J, Tsai H-D, Chou M-C and Yeh G-P 2016 Clinical application of high-intensity focused ultrasound in cancer therapy *J. Cancer* **7** 225–31
- Hsiao Y-S and Deng C X 2016 Calibration and evaluation of ultrasound thermography using infrared imaging *Ultrasound Med. Biol.* **42** 503–17
- Hsiao Y-S, Kumon R E and Deng C X 2013 Characterization of lesion formation and bubble activities during high-intensity focused ultrasound ablation using temperature-derived parameters *Infrared Phys. Technol.* **60** 108–17
- Huang L and Liu L-S 2009 Simultaneous determination of thermal conductivity and thermal diffusivity of food and agricultural materials using a transient plane-source method *J. Food Eng.* **95** 179–85
- Jacques S L 2013 Optical properties of biological tissues: a review *Phys. Med. Biol.* **58** R37–61
- Jacques S L and Gaeni M O 1989 Thermally induced changes in optical properties of heart *Annual Int. Conf. of the IEEE Engineering in Medicine and Biology* vol 11 pt 4 (Washington, DC: OSA Publishing) pp 1199–200
- Khokhlova T D, Pelivanov I M, Sapozhnikov O A, Solomatina V S and Karabutov A A 2006 Opto-acoustic diagnostics of the thermal action of high-intensity focused ultrasound on biological tissues: the possibility of its applications and model experiments *Quantum Electron.* **36** 1097–102
- Khokhlova V A, Shmeleva S M, Gavrilov L R, Martin E, Sathoo N and Shaw A 2013 Infrared mapping of ultrasound fields generated by medical transducers: feasibility of determining absolute intensity levels *J. Acoust. Soc. Am.* **134** 1586–97

- Kienle A, Lilge L, Patterson M S, Hibst R, Steiner R and Wilson B C 1996 Spatially resolved absolute diffuse reflectance measurements for noninvasive determination of the optical scattering and absorption coefficients of biological tissue *Appl. Opt.* **35** 2304–14
- Kim Y-S 2015 Advances in MR image-guided high-intensity focused ultrasound therapy *Int. J. Hypertherm.* **31** 225–32
- Kong F, Tang J, Lin M and Rasco B 2008 Thermal effects on chicken and salmon muscles: tenderness, cook loss, area shrinkage, collagen solubility and microstructure *LWT Food Sci. Technol.* **41** 1210–22
- Lai P, McLaughlan J R, Draudt A B, Murray T W, Cleveland R O and Roy R A 2011 Real-time monitoring of high-intensity focused ultrasound lesion formation using acousto-optic sensing *Ultrasound Med. Biol.* **37** 239–52
- Lang B H-H, Woo Y-C and Wong C K H 2017 High-intensity focused ultrasound for treatment of symptomatic benign thyroid nodules: a prospective study *Radiology* **284** 161640
- Lundt J E, Allen S P, Shi J, Hall T L, Cain C A and Xu Z 2017 Non-invasive, rapid ablation of tissue volume using histotripsy *Ultrasound Med. Biol.* **43** 2834–47
- Madding R P 2003 Emissivity measurement using infrared imaging radiometric cameras *Encyclopedia of Optical Engineering* ed R G Driggers (New York: CRC Press) pp 475–84
- Marquez G, Wang L V, Lin S-P, Schwartz J A and Thomsen S L 1998 Anisotropy in the absorption and scattering spectra of chicken breast tissue *Appl. Opt.* **37** 798–804
- McDannold N 2005 Quantitative MRI-based temperature mapping based on the proton resonant frequency shift: review of validation studies *Int. J. Hypertherm.* **21** 533–46
- Murray T W, Lai P and Roy R A 2012 Measuring tissue properties and monitoring therapeutic responses using acousto-optic imaging *Ann. Biomed. Eng.* **40** 474–85
- Myers M R and Giridhar D 2011 Theoretical framework for quantitatively estimating ultrasound beam intensities using infrared thermography *J. Acoust. Soc. Am.* **129** 4073–83
- Nagarajan V K and Yu B 2016 Monitoring of tissue optical properties during thermal coagulation of *ex vivo* tissues *Lasers Surg. Med.* **48** 686–94
- Nilsson A M K, Stureson C, Liu D L and Andersson-Engels S 1998 Changes in spectral shape of tissue optical properties in conjunction with laser-induced thermotherapy *Appl. Opt.* **37** 1256–67
- Nyborg W L 1981 Heat generation by ultrasound in a relaxing medium *J. Acoust. Soc. Am.* **70** 310–2
- Prahl S A, van Gemert M J C and Welch A J 1993 Determining the optical properties of turbid media by using the adding-doubling method *Appl. Opt.* **32** 559–68
- Ribault M, Chapelon J Y, Cathignol D and Gelet A 1998 Differential attenuation imaging for the characterization of high intensity focused ultrasound lesions *Ultrasonic Imaging* **20** 160–77
- Righetti R, Kallel F, Stafford R J, Price R E, Krouskop T A, Hazle J D and Ophir J 1999 Elastographic characterization of HIFU-induced lesions in canine livers *Ultrasound Med. Biol.* **25** 1099–113
- Ritz J P, Roggan A, Isbert C, Miller G, Buhr H J and Germer C T 2001 Optical properties of native and coagulated porcine liver tissue between 400 and 2400 nm *Lasers Surg. Med.* **29** 205–12
- Rivens I, Shaw A, Civalle J and Morris H 2007 Treatment monitoring and thermometry for therapeutic focused ultrasound *Int. J. Hypertherm.* **23** 121–39
- Sanghvi N T, Chen W-H, Carlson R, Weis C, Seip R, Uchida T and Marberger M 2017 Clinical validation of real-time tissue change monitoring during prostate tissue ablation with high intensity focused ultrasound *J. Ther. Ultrasound* **5** 24
- Sapareto S A and Dewey W C 1984 Thermal dose determination in cancer therapy *Int. J. Radiat. Oncol., Biol. Phys.* **10** 787–800
- Seip R, Tavakkoli J, Carlson R F, Wunderlich A, Sanghvi N T, Dines K A and Gardner T A 2002 High-intensity focused ultrasound (HIFU) multiple lesion imaging: comparison of detection algorithms for real-time treatment control 2002 IEEE Ultrasonics Symp., 2002. Proc. (IEEE) pp 1427–30
- Shaw A, Khokhlova V, Bobkova S, Gavrilov L and Hand J 2011 Calibration of HIFU intensity fields measured using an infra-red camera *J. Phys.: Conf. Ser.* **279** 012019
- Shi X, Martin R W, Rouseff D, Vaezy S and Crum L A 1999 Detection of high-intensity focused ultrasound liver lesions using dynamic elastometry *Ultrasonic Imaging* **21** 107–26
- Sinden D and ter Haar G 2014 Dosimetry implications for correct ultrasound dose deposition: uncertainties in descriptors, planning and treatment delivery *Transla. Cancer Res.* **3** 459–71
- Sordillo L A, Pu Y, Pratavieira S, Budansky Y and Alfano R R 2014 Deep optical imaging of tissue using the second and third near-infrared spectral windows *J. Biomed. Opt.* **19** 056004
- Souchon R, Rouvière O, Gelet A, Detti V, Srinivasan S, Ophir J and Chapelon J-Y 2003 Visualisation of HIFU lesions using elastography of the human prostate *in vivo*: preliminary results *Ultrasound Med. Biol.* **29** 1007–15
- Stepanishen P R and Benjamin K C 1982 Forward and backward projection of acoustic fields using FFT methods *J. Acoust. Soc. Am.* **71** 803–12
- Sun P and Wang Y 2010 Measurements of optical parameters of phantom solution and bulk animal tissues *in vitro* at 650 nm *Opt. Laser Technol.* **42** 1–7
- Torres J H, Welch A J, Çilesiz I and Motamedi M 1994 Tissue optical property measurements: overestimation of absorption coefficient with spectrophotometric techniques *Lasers Surg. Med.* **14** 249–57
- Umemura S and Cain C A 1989 The sector-vortex phased array: acoustic field synthesis for hyperthermia *IEEE Trans. Ultrason. Ferroelectr. Freq. Control* **36** 249–57
- Usamentiaga R, Venegas P, Guerediaga J, Vega L, Molleda J and Bulnes F 2014 Infrared thermography for temperature measurement and non-destructive testing *Sensors* **14** 12305–48
- van Rhooen G C, Samaras T, Yarmolenko P S, Dewhurst M W, Neufeld E and Kuster N 2013 CEM43°C thermal dose thresholds: a potential guide for magnetic resonance radiofrequency exposure levels? *Eur. Radiol.* **23** 2215–27
- Vappou J, Bour P, Marquet F, Ozenne V and Quesson B 2018 MR-ARFI-based method for the quantitative measurement of tissue elasticity: application for monitoring HIFU therapy *Phys. Med. Biol.* **63** 095018
- Yu Y, Shen G, Zhou Y, Bai J and Chen Y 2013 Quantitative assessment of acoustic intensity in the focused ultrasound field using hydrophone and infrared imaging *Ultrasound Med. Biol.* **39** 2021–33
- Zhao J, Zhao Q, Jiang Y, Li W, Yang Y, Qian Z and Liu J 2018 Feasibility study of modeling liver thermal damage using minimally invasive optical method adequate for *in situ* measurement *J. Biophoton.* **11** e201700302
- Zhong H, Wan M-X, Jiang Y-F and Wang S-P 2007 Monitoring imaging of lesions induced by high intensity focused ultrasound based on differential ultrasonic attenuation and integrated backscatter estimation *Ultrasound Med. Biol.* **33** 82–94
- Zhu M, Sun Z and Ng C K 2017 Image-guided thermal ablation with MR-based thermometry *Quant. Imaging Med. Surg.* **7** 356–68